

The Deepest Radio Study of the Pulsar Wind Nebula G21.5–0.9: Still No Evidence for the Supernova Shell

M. F. Bietenholz^{1,2}, H. Matheson³, S. Safi-Harb^{3,4}, C. Brogan⁴, and N. Bartel²

¹*Hartebeesthoek Radio Observatory, PO Box 443, Krugersdorp, 1740, South Africa*

²*Department of Physics and Astronomy, York University, Toronto, M3J 1P3, Ontario, Canada*

³*Department of Physics and Astronomy, University of Manitoba, Winnipeg, Manitoba, Canada*

⁴*Canada Research Chair*

⁵*NRAO, 520 Edgemont Rd, Charlottesville, VA, 22903, USA*

3 November 2021

ABSTRACT

We report on sensitive new 1.4-GHz VLA radio observations of the pulsar wind nebula G21.5–0.9, powered by PSR J1833–1034, and its environs. Our observations were targeted at searching for the radio counterpart of the shell-like structure seen surrounding the pulsar wind nebula in X-rays. Some such radio emission might be expected as the ejecta from the $\lesssim 1000$ yr old supernova expand and interact with the surrounding medium. We find, however, no radio emission from the shell, and can place a conservative 3σ upper limit on its 1-GHz surface brightness of $7 \times 10^{-22} \text{ W m}^{-2} \text{ Hz}^{-1} \text{ sr}^{-1}$, comparable to the lowest limits obtained for radio emission from shells around other pulsar-wind nebulae. Our widefield radio image also shows the presence of two extended objects of low-surface brightness. We re-examine previous 327-MHz images, on which both the new objects are visible. We identify the first, G21.64–0.84, as a new shell-type supernova remnant, with a diameter of $\sim 13'$ and an unusual double-shell structure. The second, G21.45–0.59, $\sim 1'$ in diameter, is likely an HII region.

Key words: supernova remnants

1 INTRODUCTION

The crab-like supernova remnant G21.5–0.9 (SNR 021.5–00.9) harbours a pulsar wind nebula (PWN), powered by the 61.86 ms pulsar, PSR J1833–1034. Despite having a high spin-down luminosity of $3.3 \times 10^{37} \text{ erg s}^{-1}$ PSR J1833–1034 produces only faint pulsed emission, and was only recently discovered (Gupta et al. 2005; Camilo et al. 2006). Radio imaging of the PWN spanning a ~ 15 -year period has shown that it is expanding quite rapidly, having an expansion age of 870_{-150}^{+200} yr (Bietenholz & Bartel 2008), making PSR J1833–1034 one of the youngest pulsars known. Using a determination of the hydrogen column density, CO and HI measurements, Camilo et al. (2006) determined that the distance to G21.5–0.9 was 4.7 ± 0.4 kpc, which is consistent with earlier determinations (e.g. Safi-Harb et al. 2001; Davelaar et al. 1986). We will adopt the value of 4.7 kpc.

The PWN is bright in both the radio and X-ray, having luminosities of $\sim 10\%$ and $\sim 1\%$ respectively of those of the Crab Nebula.

Recent radio images of G21.5–0.9 show a flat-spectrum PWN, with an angular diameter of $\sim 1'$ (Bietenholz & Bartel 2008), which has filamentary structure similar to that seen in the Crab Nebula. The pulsar is expected to have

been born in a supernova explosion, and since it is quite young, one might expect to see some emission associated with the expanding shell of supernova ejecta. However, despite a number of studies in the radio (Becker & Kundu 1976; Wilson & Weiler 1976; Becker & Szymkowiak 1981; Morsi & Reich 1987; Fürst et al. 1988; Kassim 1992; Bock et al. 2001; Bietenholz & Bartel 2008), no radio emission from the supernova shock front has been seen. In particular, the 1-GHz surface brightness, $\Sigma_{1 \text{ GHz}}$, of any such emission has been limited (1σ) to being $< 4 \times 10^{-21} \text{ W m}^{-2} \text{ Hz}^{-1} \text{ sr}^{-1}$ (Slane et al. 2000). Although this limit represents much brighter emission than the faintest known supernova shell in our Galaxy, G156.2+5.7, which has $\Sigma_{1 \text{ GHz}} = 5.8 \times 10^{-23} \text{ W m}^{-2} \text{ Hz}^{-1} \text{ sr}^{-1}$ (Reich et al. 1992), G21.5–0.9 is much younger¹ and therefore might be expected to have brighter radio emission assuming a similar ISM density and supernova explosion energy.

G21.5–0.9’s centrally-condensed PWN is also seen clearly in X-rays (Slane et al. 2000; Safi-Harb et al. 2001; Warwick et al. 2001; Matheson & Safi-Harb 2005;

¹ For G156.2+5.7, Yamauchi et al. (1999) give an age of 15,000 yr and a distance of 1.3 kpc, but we note that both these values are uncertain by a factor of ~ 2 .

Bocchino et al. 2005; Matheson & Safi-Harb 2010). In contrast to the radio, however, a fainter “halo” of X-ray emission, with a radius of $\sim 150''$, is indeed seen surrounding the PWN. Both Matheson & Safi-Harb (2005) and Bocchino et al. (2005) argue that most of this halo X-ray emission is not from the outer shock, but is rather due to dust scattering. However, a relatively weak, limb-brightened X-ray component is also seen on the eastern side, which has been interpreted as non-thermal emission associated with the supernova shock (Bocchino et al. 2005; Matheson & Safi-Harb 2010).

With the goal of identifying any radio emission associated with this non-thermal X-ray emission from the forward shock, we obtained sensitive new observations of G21.5–0.9 and its surroundings.

2 OBSERVATIONS AND DATA REDUCTION

We observed G21.5–0.9 in the 1.4 GHz band on 2008 March 17, using the C array configuration of the National Radio Astronomy Observatory² (NRAO) VLA, with a total time of 6 hours. In this array configuration, the VLA is sensitive to structures up to $15'$ in size, so the structure of the putative radio-shell around G21.5–0.9 should be well-sampled. In order to maximise the field-of-view, u - v coverage and dynamic range, we observed in spectral line mode using spaced centre frequencies of 1.4649 and 1.3851 GHz in the two intermediate-frequency (IF) channels. We phase-referenced our observations to the compact source PMN J1832–1035, whose position is accurate to better than $1''$, therefore our astrometric uncertainty is dominated by contributions from noise and errors in phase-referencing. We estimate our astrometric uncertainty at $< 4''$. Our flux density scale was set from observations of 3C 48 and 3C 286. The data reduction was carried out using standard procedures from NRAO’s AIPS software package.

Our final images were made from self-calibrated visibility data, using CLEAN deconvolution with multiple non-coplanar facets. Since our two IF frequencies differ by $\sim 6\%$, sources with different spectral indices could show noticeable differences in relative brightness between the two IFs. In particular, in Bietenholz & Bartel (2008) we found that the spectral index, α (where the flux density S at frequency ν is $\propto \nu^\alpha$), of the G21.5–0.9 PWN is quite uniform over the nebula, with a value of $+0.08^{+0.06}_{-0.09}$. In contrast to a PWN, a supernova shell would be expected to have a notably steeper spectrum, with a typical value of $-0.8 \sim -0.4$ (Green 2009).

In order that such spectral-index differences not limit the dynamic range in the deconvolved image, we chose to image and deconvolve our two IFs separately. We then averaged the resulting two images to obtain our final, combined image. The final image should correctly represent the brightness at the mean frequency of 1.43 GHz regardless of the spectral index. Separate imaging of the two IFs did in fact produce a slightly higher dynamic range than did combining the two IFs before the Fourier transform stage.

² The National Radio Astronomy Observatory, NRAO, is a facility of the National Science Foundation operated under cooperative agreement by Associated Universities, Inc.

We also discuss 327 MHz images of this region resulting from earlier VLA observations of a large segment of the Galactic plane. These 327-MHz observations were taken as part of an effort to survey the inner Galactic plane at low radio frequencies, and are described in Brogan et al. (2006, 2005). The FWHM resolution is $85''$. A lower-resolution image made from these data, which covers the part of the plane relevant to this paper, is reproduced in Brogan et al. (2005).

Finally we also discuss a *Chandra* X-ray image of G21.5–0.9 and its environs, produced by combining a total of ~ 520 ksec of *Chandra* observations in the energy range 0.2 to 10 keV. The X-ray data are described in Matheson & Safi-Harb (2005, 2010).

3 RESULTS: 1.4-GHZ WIDE-FIELD IMAGE

We show the wide-field radio-image of the G21.5–0.9 region in the top part of Fig. 1. This image represents only part of the imaged area, chosen to show the sources of interest. We further chose the range of greyscale in order to show the weaker sources, with the result that the stronger ones such as G21.5–0.9 itself are saturated. Clearly visible in this image is the feature called the “northern knot”, $\sim 2'$ to the north of the centre of G21.5–0.9. This image is corrected for the response of the primary beam (which has a FWHM of $31'$ at 1.43 GHz). As a consequence the rms background level increases with distance from the pointing centre. Near G21.5–0.9, the rms background brightness was $\sim 260 \mu\text{Jy bm}^{-1}$. This is the deepest radio image so far obtained of G21.5–0.9 and its surroundings. The bottom part of Fig. 1 shows the *Chandra* X-ray image for the same field.

In addition to G21.5–0.9 there are a number of other sources visible. The brightest is QSO J1832–105, with a 1.43-GHz flux density of 1.07 Jy. Two other resolved sources are visible at approximately RA = $18^{\text{h}} 33^{\text{m}} 2^{\text{s}}$, decl. = $-10^{\circ} 27' 0''$ and RA = $18^{\text{h}} 32^{\text{m}} 4^{\text{s}}$, decl. = $-10^{\circ} 28' 3''$. We call these sources G21.64–0.84 and G21.45–0.59, as they are likely both Galactic, and we will discuss them below. There are also a number of weaker unresolved sources visible, which are likely extragalactic and which we do not discuss further.

Also present in the full image and included in the deconvolution and self-calibration was the supernova remnant Kes 69, which is to the northwest of G21.5–0.9. We choose to exclude Kes 69 from the portion of the image displayed in Fig. 1, as it is beyond the 25% point of the primary beam, and the image details are not reliable (see Kassim 1992, for a radio image of Kes 69). Some artifacts are visible in the western and northwester parts of the image, due to J1832–105 and Kes 69.

3.1 G21.5–0.9

In Fig. 2 we show a detail of the radio image showing the G21.5–0.9 PWN. The image corresponds well, albeit at lower resolution, to the one of Bietenholz & Bartel (2008). G21.5–0.9 had a total 1.43-GHz flux density of 7.0 ± 0.4 Jy, with a peak surface brightness at our resolution of $0.62 \pm 0.03 \text{ Jy bm}^{-1}$, corresponding to a brightness temperature of 1500 ± 75 K (where the uncertainties are dominated by the assumed 5% uncertainty in the flux-density calibration).

On our 327 MHz image (image not reproduced here;

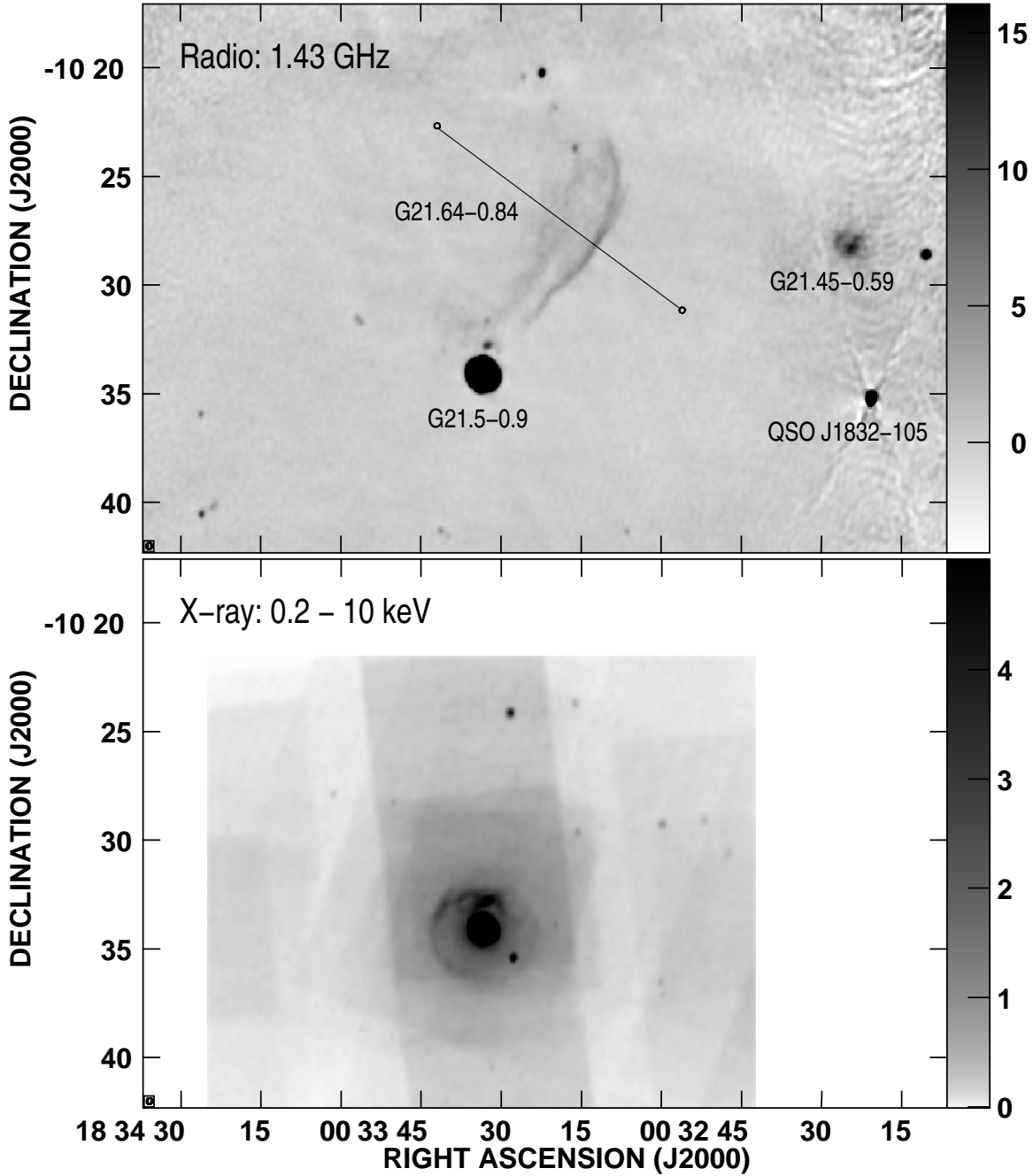


Figure 1. Top: a wide-field 1.4-GHz radio image of the region around G21.5–0.9. The greyscale range of -2 to 10 mJy bm^{-1} was chosen to emphasise any weaker background emission, therefore saturating the G21.5–0.9 PWN itself, which had a peak brightness of 621 mJy bm^{-1} . The sources we discuss in the text are labelled. The image has been corrected for the VLA primary beam response, with the result that the rms is ~ 260 $\mu\text{Jy bm}^{-1}$ near G21.5–0.9, which was the pointing centre, and increases with increasing distance away from it. The FWHM of the convolving beam was $18.1'' \times 13.8''$ at p.a. -12° . Low-level artifacts are visible in the vicinity of the bright source, QSO J1832–105. The diagonal line segment shows the location and orientation of the slice through G21.64–0.84 shown in Fig. 4. **Bottom:** An X-ray image of G21.5–0.9, showing the same field of view, and convolved to the same resolution, as the radio image above, made by combining a total of ~ 520 ksec of *Chandra* observations in the energy range 0.2 to 10 keV (for details, see Matheson & Safi-Harb 2010). The greyscale is chosen so that the G21.5–0.9 PWN in the centre is saturated in order to show the fainter X-ray emission surrounding it. Different regions of the image have been observed with different effective exposure times, resulting in a varying background level. The bright point source in the south-western part of the X-ray halo is an unrelated emission-line star, SS 397.

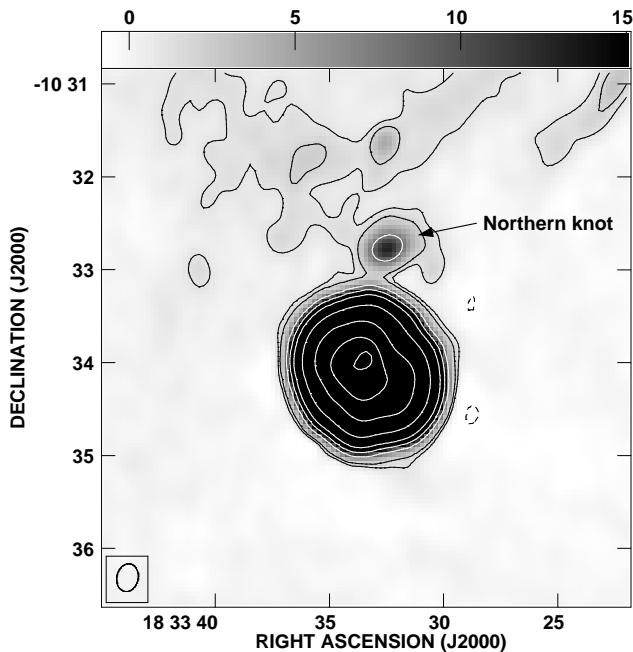


Figure 2. A 1.4-GHz image of G21.5–0.9. The figure represents a detail of the top panel of Fig. 1. The contours are drawn at $-1, 1, 2, 4, 8, 16, 32, 100, 300, 500$ and $600 \text{ mJy } \text{bm}^{-1}$. The greyscale is chosen to emphasise the fainter emission, and is labelled in $\text{mJy } \text{bm}^{-1}$. The convolving beam FWHM, indicated at lower left, was $18.8'' \times 13.8''$ at p.a. -12° . The peak brightness in this sub-image was $621 \text{ mJy } \text{bm}^{-1}$, and the rms background noise was $260 \mu\text{Jy } \text{bm}^{-1}$. The “northern knot” is labelled. Also visible at the top of the image is the lower portion of G21.64–0.84.

see Brogan et al. 2005), G21.5–0.9 is also clearly visible, although only marginally resolved. Comparison of the flux density of $7.3 \pm 0.7 \text{ Jy}$ determined from the 327-MHz image with that at 1.4 GHz yields an integrated spectral index between these frequencies, $\alpha_{0.3 \text{ GHz}}^{1.4 \text{ GHz}}$, of 0.0 ± 0.1 , consistent with other determinations of G21.5–0.9’s radio spectral index (e.g., Bietenholz & Bartel 2008).

There is a relatively compact radio source, approximately $1'$ to the north of the main body of G21.5–0.9, which corresponds to the X-ray feature called the “northern knot”³ (e.g., Matheson & Safi-Harb 2010). B. Gaensler, in a private communication, reported seeing the northern knot in earlier 1.4-GHz radio observations. The northern knot has a total 1.43-GHz flux density of $20.2 \pm 1.8 \text{ mJy}$, and is marginally resolved in our image, with an intrinsic FWHM size, as estimated by an elliptical Gaussian fit, of $18'' \times 8''$ at p.a. 105° . The peak brightness position in the radio is consistent with that seen in the X-ray when the latter is convolved to the same resolution, as can be seen in the top and bottom panels of Fig. 1.

The northern knot is not discernible on our lower-resolution 327 MHz image, being blended with G21.5–0.9 itself. The knot is marginally visible in an image made from the 5-GHz data of Bietenholz & Bartel (2008)⁴. We esti-

mate a total 5-GHz flux density for the northern knot of $19 \pm 7 \text{ mJy}$, resulting a nominal value for the knots spectral index, $\alpha_{1.4 \text{ GHz}}^{4.9 \text{ GHz}}$, of -0.04 , similar to that body of G21.5–0.9. However, the uncertainties on the spectral index are large, and the $p = 2.3\%$ (2σ) limits on $\alpha_{1.4 \text{ GHz}}^{4.9 \text{ GHz}}$ are -1.3 and $+0.5$.

What is notably absent from our deep 1.4-GHz image is radio emission corresponding to the limb-brightened X-ray emission visible in the bottom panel of Fig. 1. Although some diffuse radio emission appears north of the northern knot, we believe that it is not the counterpart of the X-ray shell of G21.5–0.9, but more likely associated with G21.64–0.84, which we discuss below. We derive a new upper limit to the radio emission from the SNR shell in § 4.1.

3.2 G21.64–0.84

A so far uncatalogued source, G21.64–0.84, is distinctly visible in the 1.4-GHz image in Fig. 1. It is a large elongated structure, which extends from near G21.5–0.9 to the north-northwest. It is brightest in the middle, reaching a peak 1.43-GHz brightness of $6.8 \pm 0.5 \text{ mJy } \text{bm}^{-1}$ (corresponding to a brightness temperature of $17 \pm 1 \text{ K}$). It has a total length of $\sim 10'$. It seems to consist of two relatively distinct and roughly parallel curved ridges of emission, with the western or outer one being better defined, and the eastern or inner one being more diffuse and $\sim 1.5'$ distant. The total 1.43-GHz flux density in the G21.64–0.84 is $660 \pm 50 \text{ mJy}$, with each of the two ridges having approximately half the total.

G21.64–0.84 is also visible in the 327 MHz image, and we show a detail in Fig. 3. At this frequency, due to the larger primary beam, much more of the source is visible than at 1.4 GHz, and it can be seen to be a relatively circular shell-structure. The centre of the shell is at RA = $18^{\text{h}} 33^{\text{m}} 6^{\text{s}}$ and decl. $-10^\circ 25' 4''$, or at $l = 21.64, b = -0.84$. Our name for this source, G21.64–0.84, is based on the centre position of the shell as seen at 327 MHz. The outer angular diameter of the shell is $\sim 13'$. The total flux density at 327 MHz is 2.8 Jy , with an estimated uncertainty of $\sim 0.5 \text{ Jy}$ due to the somewhat uncertain zero-level in the images. The 327-MHz flux density of the part visible in the 1.4 GHz image is $1.4 \pm 0.2 \text{ mJy}$, and over this region the integrated value of $\alpha_{0.3 \text{ GHz}}^{1.4 \text{ GHz}}$ is -0.5 ± 0.1 . A somewhat steeper spectrum is suggested for the northern and eastern sides of the shell, which are not visible at 1.4 GHz, however due to the uncertain zero-levels and low signal-to-noise ratios, a constant value of $\alpha_{0.3 \text{ GHz}}^{1.4 \text{ GHz}} \sim -0.6$ for the whole shell is probably not excluded. The averaged over the whole of the 327-MHz surface brightness is $2.5 \times 10^{-21} \text{ W m}^{-2} \text{ Hz}^{-1} \text{ sr}^{-1}$, and if we take $\alpha = -0.5$, then $\Sigma_{1 \text{ GHz}} = 1.4 \times 10^{-21} \text{ W m}^{-2} \text{ Hz}^{-1} \text{ sr}^{-1}$.

We include the G21.64–0.84 region in the wide-field X-ray image shown in the lower panel of Fig. 1 above. Although this region was not the primary target, and the instrumental background differs in different parts of G21.64–0.84, no sign of X-ray emission which might be associated with G21.64–0.84 is seen down to limits of 10^{-3} times the peak brightness of G21.5–0.9. At the radio peak-brightness position of G21.64–0.84, we estimate that the X-ray exposure was $\sim 130 \text{ ks}$.

³ This feature was also called the “northern spur” by Bocchino et al. (2005)

⁴ Note that the northern knot is not within the portion of the im-

age reproduced in Bietenholz & Bartel (2008). We have re-imaged the visibility data to include the knot region.

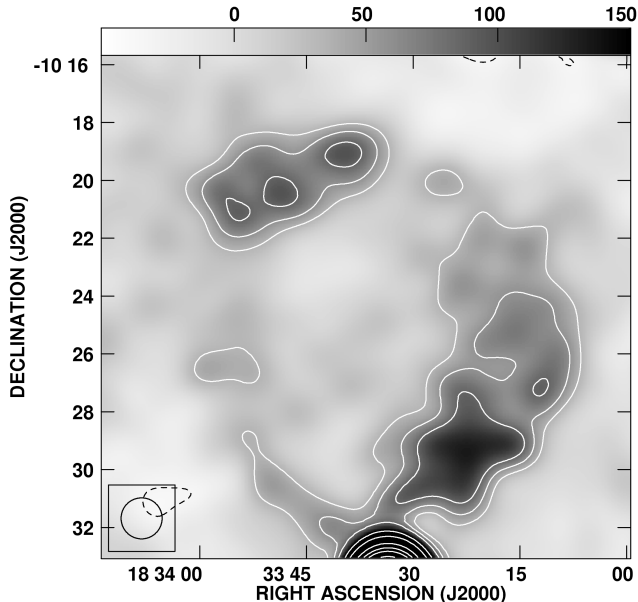


Figure 3. A 327 MHz image of G21.64–0.84. The FWHM resolution was $85''$, and is indicated at lower left. The greyscale is labelled in mJy bm^{-1} , and the rms background was $\sim 14 \text{ mJy bm}^{-1}$. The contours are drawn at $-0.6, 0.6, 1, 1.5, 3.0, 5, 10, 15, 20,$ and 30% of the peak brightness which was 5.73 Jy bm^{-1} . G21.5–0.9 is partly visible at the bottom of the image.

In Fig. 4, we show a profile through G21.64–0.84 centred at $18^{\text{h}} 33^{\text{m}} 12^{\text{s}}, -10^{\circ} 28' 09''.3$, which is near its peak brightness position (the location of the profile is indicated in Fig. 1). The profile through the brighter ridge is asymmetric, with the north-east side being approximately half as steep as the southwest one. In particular, along the slice direction, the half-maximum point in the northeast direction is reached at a distance of $20''$ from the peak, whereas in the southwest direction it is reached at a distance of $11''$. The FWHM on the slice is therefore $31''$, which is notably larger than our resolution of $\sim 13''$ along the slice direction. The intrinsic FWHM is therefore close to the observed one of $31''$. The more diffuse, fainter ridge has a FWHM of $\sim 3'$. We discuss the nature of G21.64–0.84 below in § 4.2.

3.3 G21.45–0.59

A further weak resolved source is visible in both our 1.4-GHz (Fig. 1) and 327-MHz images near RA $18^{\text{h}} 32^{\text{m}}$, decl. $= -10^{\circ} 28'$ ($l = 21.459, b = -0.59$), which we call G21.45–0.59. It is approximately 1.5 in diameter. Its 327-MHz peak brightness was $209 \pm 24 \text{ mJy bm}^{-1}$ (at $85''$ resolution), corresponding to a brightness temperature of $330 \pm 38 \text{ K}$.

We estimate total flux densities for G21.45–0.59 of $\sim 0.3 \text{ Jy}$ at 1.4 GHz and $\sim 0.5 \text{ Jy}$ at 327 MHz, corresponding to $\alpha_{0.3 \text{ GHz}}^{1.4 \text{ GHz}} \sim -0.3$, although this spectral index estimate should be treated with caution as the total flux densities are rather uncertain because of the uncertain extent of the source and zero-levels, as well as the large primary-beam correction factor of ~ 2.6 at 1.4-GHz.

G21.45–0.59 has likely been identified already in the 2.7-GHz continuum survey of the Galactic plane by

Reich et al. (1984), who list the source RFS 323 at a position about $90''$ away from our peak brightness position for G21.45–0.59, and having a total 2.7-GHz flux density of $0.50 \pm 0.15 \text{ Jy}$. The position offset between G21.45–0.59 and RFS 232 is larger than either our own astrometric uncertainty of $< 4''$ or that of $20''$ listed by Reich et al. (1984). However, the FWHM resolution of the Reich et. al survey was $4.3'$, so the positional offset is only approximately $1/3$ the Reich et al. beamwidth, and thus probably not significant. We consider that RFS 232 can thus be identified with G21.45–0.59, with Reich et al.’s 2.7-GHz flux density implying $\alpha_{0.3 \text{ GHz}}^{2.7 \text{ GHz}} \sim 0$.

We note that G21.45–0.59 is also visible in the 1.4-GHz VLA Galactic Plane Survey (VGPS Stil et al. 2006), and has a peak brightness position consistent to within $2''$ with the one we measured at that frequency. We consider our peak brightness position for G21.45–0.59 more reliable than that listed for RFS 232 by Reich et al. (1984).

Our X-ray observations do not extend to G21.45–0.59, so its X-ray brightness is unknown. We will discuss the nature of G21.45–0.59 in § 4.3 below.

4 DISCUSSION

4.1 G21.5–0.9 and Limits on Radio Emission from its Forward Shock

Our 1.4-GHz radio image of the G21.5–0.9 region (Fig. 1, top) is dominated by the pulsar-wind nebula G21.5–0.9. Our observations are sensitive to structures much larger than the G21.5–0.9 PWN, so there is no reason to suspect any significant deficit in the recovered flux density due to missing short interferometer spacings. Indeed, our total recovered flux density of $7.0 \pm 0.4 \text{ Jy}$ is consistent within the uncertainties with the value measured by Altenhoff et al. (1970) and the radio spectrum compiled by Salter et al. (1989).

Except for the northern knot, no radio emission is visible which can be associated with the X-ray halo or the limb-brightened feature seen in X-ray. Conservatively scaling the rms background brightness of our image ($260 \mu\text{Jy bm}^{-1}$ at 1.43 GHz) to the standard frequency of 1 GHz using a steep assumed spectral index⁵ we obtain a 3σ upper limit on $\Sigma_{1\text{GHz}}$ of $1.6 \times 10^{-21} \text{ W m}^{-2} \text{ Hz}^{-1} \text{ sr}^{-1}$.

Since the X-ray limb detected at a radius of $\sim 150''$ likely indicates the location of the forward shock (see Bocchino et al. 2005; Matheson & Safi-Harb 2010), we can place more stringent limits on the radio brightness of the shell by integrating over the shell region. Over an annular region with an outer angular radius of $150''$ and a thickness of 20% of the outer radius, the observed total 1.43-GHz flux density is $12 \pm 6 \text{ mJy}$, with a 3σ upper limit of 30 mJy , corresponding to an average 1.43-GHz spectral luminosity of $< 8 \times 10^{20} \text{ erg s}^{-1} \text{ Hz}^{-1} (D/4.7\text{kpc})$ or a surface brightness

⁵ To determine the limit, we use $\alpha = -0.8$ as the steepest reasonable spectrum for a shell. As the difference between the observed frequency of 1.43 GHz and the nominal one is not large, our result is not sensitive to reasonable changes in α , for example, using a more usual value of $\alpha = -0.5$ would lower our 3σ surface brightness limit by $\sim 8\%$ to $1.4 \times 10^{-21} \text{ W m}^{-2} \text{ Hz}^{-1} \text{ sr}^{-1}$.

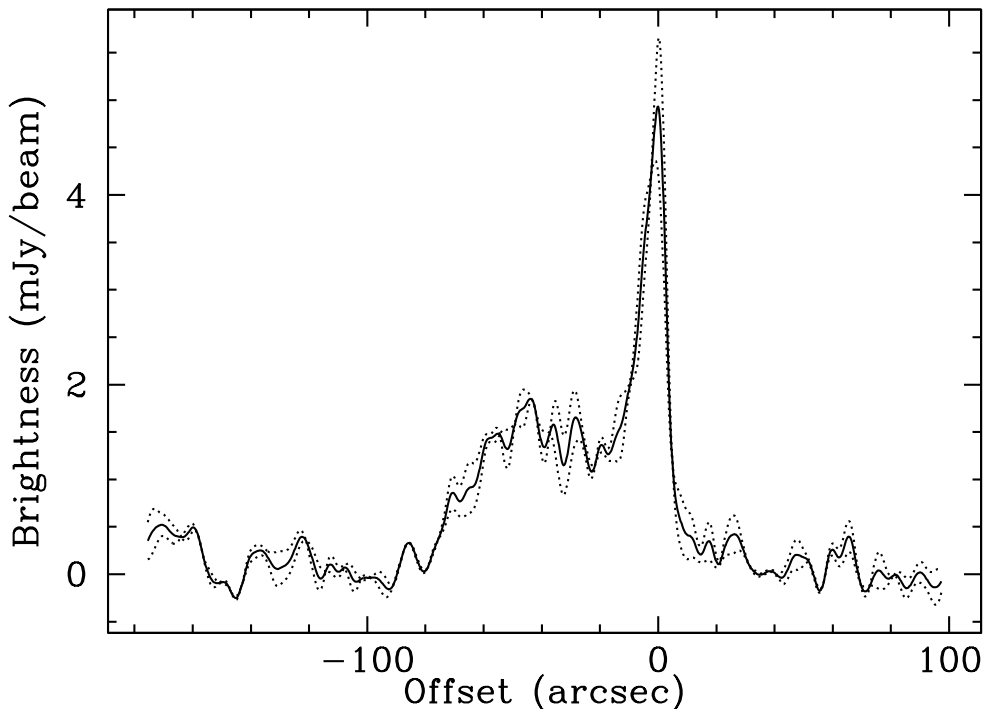


Figure 4. A profile drawn through G21.64–0.84, at p.a. = -127° taken from the image shown in Fig. 1, where the location of the slice is also shown. The offsets are in arc-seconds, measured from the slice peak, with a positive offset being to the southwest. To increase the signal-to-noise, we averaged three parallel slices, each displaced by $\pm 7''$ transverse to the slice direction. The solid line shows this average value, while the dotted lines indicate the rms over the three slices. The slice peak is $5.03 \text{ mJy beam}^{-1}$, and it is located at $18^{\text{h}} 33^{\text{m}} 12^{\text{s}}$, $-10^\circ 28' 09''.3$. The half-power points occur at displacements of $-20''$ and $+11''$ from this peak.

of $< 1.2 \mu\text{Jy}$ per square arc-second. Again conservatively scaling to 1 GHz with $\alpha = -0.8$ results in a 3σ limit on the average surface of $\Sigma_{1 \text{ GHz}} < 7 \times 10^{-22} \text{ W m}^{-2} \text{ Hz}^{-1} \text{ sr}^{-1}$. Our assumption for the shell geometry is conservative: for shells thicker than 20%, as might be expected for an age of 870 yr (see, e.g., Jun & Norman 1996; Chevalier 1982), the surface-brightness limit would be lower. In addition, as noted above, for values of α flatter than the assumed -0.8 , the limit would also be slightly lower, with $\alpha = -0.5$ resulting in a value of $6 \times 10^{-22} \text{ W m}^{-2} \text{ Hz}^{-1} \text{ sr}^{-1}$ for the limit. Finally, the annular region above includes real emission due to G21.64–0.84, which is probably not associated with G21.5–0.9. If we exclude this contribution, the limit on the average surface brightness decreases by approximately 20%.

The limit on the radio surface brightness of G21.5–0.9’s shell, which corresponds to $< 6 \times 10^{-4}$ times the peak surface brightness of the PWN, is ~ 17 times lower than those previously obtained for G21.5–0.9 (Slane et al. 2000).

It is expected that the shocks formed as the shell of supernova ejecta plough through the interstellar medium would both accelerate particles and amplify the ambient magnetic field by compression and through instabilities. Radio emission from this region might therefore be expected, especially for a remnant as young as G21.5–0.9. Where then is this radio emission?

We note first that G21.5–0.9 is not unique in having no detectable radio emission from the supernova shell. In fact, most other young PWNs seem to show little radio emis-

sion from the putative shell, with the best studied example being the Crab Nebula, which is one of the youngest known and also one of the very few identified with a supernova (SN 1054), and which does not have any radio emission from the ejecta shell down to a 3σ upper limit of $7.5 \times 10^{-22} \text{ W m}^{-2} \text{ Hz}^{-1} \text{ sr}^{-1}$ (Frail et al. 1995). 3C 58, also a young PWN, also has no detectable radio emission from the shell to a 3σ surface brightness limit of $\lesssim 5 \times 10^{-22} \text{ W m}^{-2} \text{ Hz}^{-1} \text{ sr}^{-1}$ (Reynolds & Aller 1985; Bietenholz et al. 2001). In other words, the present limits on the radio surface brightness of G21.5–0.9’s shell, although low, are not unusual when compared to those for other bright PWNs. What is unusual about G21.5–0.9, however, is that unlike either the Crab or 3C 58⁶, X-ray emission from which can reasonably be attributed to the forward shock *has* been detected (Bocchino et al. 2005; Matheson & Safi-Harb 2010). Matheson & Safi-Harb (2010) fit the X-ray spectrum of the limb after subtracting the halo emission, in other words the non-thermal part of the X-ray emission thought to be due to the forward shock, with broad-band models consisting of a power-law with an exponential high-energy cutoff (model *srcut*, Reynolds 1998). Using an assumed radio spec-

⁶ We note that a shell of thermal X-ray emission was seen in 3C 58 by Gotthelf et al. (2007). The diameter of ~ 5.6 pc of this shell is smaller than the maximum extent of the PWN, which is ~ 8.5 pc. The thermal X-ray emission is therefore likely associated with supernova ejecta swept up by the expanding PWN rather than the original forward shock from the supernova.

tral index of $\alpha = -0.5$, their best fit model would imply $\Sigma_{1\text{ GHz}} = 2.3 \times 10^{-22} \text{ W m}^{-2} \text{ Hz}^{-1} \text{ sr}^{-1}$, which is well below our measured 3σ limit of $7 \times 10^{-22} \text{ W m}^{-2} \text{ Hz}^{-1} \text{ sr}^{-1}$. The absence of radio emission from G21.5–0.9’s forward shock is therefore consistent with the observed non-thermal X-ray emission.

Although we detect no radio emission from the shell, we do clearly detect G21.5–0.9’s northern knot in our deep 1.4-GHz image. A marginal detection at 4.8 GHz results in a nominal spectral index, $\alpha_{1.4\text{ GHz}}^{4.9\text{ GHz}}$, of ~ 0 , albeit with large uncertainties. This nominal value of $\alpha_{1.4\text{ GHz}}^{4.9\text{ GHz}}$ is similar to that for the body of G21.5–0.9, suggesting that the knot, like the body of G21.5–0.9, consists of electrons energised by the pulsar. However, the alternate hypothesis of the knot consisting of electrons accelerated in the forward shock and having $\alpha_{1.4\text{ GHz}}^{4.9\text{ GHz}} \sim -0.5$ is not excluded by the data, so no firm conclusions as to its nature can be drawn..

4.2 G21.64–0.84: A New Shell Supernova Remnant

We have identified a new shell-like radio source in our radio images, which we have called G21.64–0.84. In the high-resolution 1.4-GHz image (Fig. 1 top), only the western part of the shell is visible, but most of the shell can be seen in the 327 MHz image (Fig. 3). Its radio spectral index of ~ -0.6 (§ 3.2) is consistent with those seen for shell-type SNRs (see, e.g., Green 2009).

We examined the $8\text{ }\mu\text{m}$ infra-red images from the Spitzer Glimpse survey (Benjamin et al. 2003), and find no infra-red emission for G21.64–0.84, which implies that G21.64–0.84 is unlikely to be either an HII region or a wind blown bubble, which latter often have a shell-like structure but are almost inevitably accompanied by infra-red emission (e.g., Brogan et al. 2006). It seems most probable that G21.64–0.84 is an as-yet uncatalogued supernova remnant.

We noted in § 3.2 above that no X-ray emission is seen from G21.64–0.84 to levels of $\sim 0.1\%$ of the peak brightness of G21.5–0.9. The lack of X-ray detection, however, does not argue against the supernova remnant hypothesis: Green (2009) has a comprehensive list of Galactic SNRs and finds that only $\sim 40\%$ of them are detected in X-ray, with high absorption in the X-ray being seen for many.

Could G21.64–0.84 represent the radio emission associated with the forward shock in G21.5–0.9, the searched for which motivated the observations? We think this possibility very unlikely, as the centre of the new shell is clearly displaced from the G21.5–0.9 PWN. If PSR J1833–1034 had been at the center of the newly-identified radio shell 870 yr ago, then its average speed since then must have $\sim 15,000 \text{ km s}^{-1}$, which is far higher than the speeds seen for pulsars. Moreover, X-ray emission from G21.5–0.9’s forward shock has in fact been identified, and is not coincident with G21.64–0.84. We therefore identify G21.64–0.84 as a previously unidentified shell-type SNR, which is unrelated to G21.5–0.9.

SNR shells typically have steeper brightness gradients at their outside edges than the inside ones, thus naturally explaining the asymmetry in the profile (Fig. 4). Although the partial double-shell morphology is not common for supernova remnants, other remnants with similar structure have been observed (see e.g., Gaensler 1998; Giacani et al. 2009).

We found that G21.64–0.84 has an average surface brightness of $\Sigma_{1\text{ GHz}} \simeq 1.4 \times 10^{-21} \text{ W m}^{-2} \text{ Hz}^{-1} \text{ sr}^{-1}$. This SNR is therefore near the peak of the observed distribution of $\Sigma_{1\text{ GHz}}$ values in the catalogue of Green (2009), but below his estimated completeness limit of $\simeq 1 \times 10^{-20} \text{ W m}^{-2} \text{ Hz}^{-1} \text{ sr}^{-1}$. We note that the catalogued number of supernova remnants in the Galaxy ($n = 274$ in the catalogue of Green 2009) is lower than the ~ 1000 generally expected from supernova rates (e.g., Tammann et al. 1994, see also discussion in Brogan et al. 2006), suggesting that there likely are many more supernova remnants to be discovered at these sensitivity levels.

A relationship has been observed between the surface-brightness and the diameter (D) for SNRs. Although this $\Sigma - D$ relation has in the past often been used to determine SNR distances it has been shown to be only of limited value for this purpose, (see, e.g., Green 2004, 2005; Bandiera & Petruk 2010). If we take $\Sigma_{1\text{ GHz}} = 1.4 \times 10^{-21} \text{ W m}^{-2} \text{ Hz}^{-1} \text{ sr}^{-1}$ for G21.64–0.84 and compare it to the sample of 47 SNRs of known distance shown in Green (2004), we can conclude only that the G21.64–0.84’s diameter is likely between 10 and 100 pc, and its distance therefore in the not very restrictive range of $3 \sim 30 \text{ kpc}$. The lack of apparent X-ray emission suggests high absorption and therefore perhaps argues against the shorter end of this range.

4.3 G21.45–0.59: A Probable HII Region

Our wide-field 1.4-GHz image also shows a relatively faint extended radio source which we have called G21.45–0.59. Unlike G21.64–0.84, it does not have a clear shell-like morphology. Although the current data do not reliably determine its radio spectral index, a relatively flat spectrum, with α in the range of -0.3 to 0 is suggested (§ 3.3). The source is present on the Glimpse $8\text{ }\mu\text{m}$ infrared images, and listed as G021.4571–00.5894 in the GLIMPSEII source list⁷. We therefore tentatively identify G21.45–0.59 as an HII region.

5 SUMMARY AND CONCLUSIONS

1. We present a new deep 1.4-GHz radio image of the PWN G21.5–0.9 and its environs. We also show a deep X-ray image, made from 520 ksec of *Chandra* data, of the same region.
2. Although the G21.5–0.9 PWN is clearly visible in our 1.4-GHz image, we see no sign of shell radio emission from the supernova forward shock. We place a 3σ upper limit of $7 \times 10^{-22} \text{ W m}^{-2} \text{ Hz}^{-1} \text{ sr}^{-1}$ on the 1-GHz surface brightness of any such emission, in particular also on any radio emission corresponding to the limb-brightened, non-thermal X-ray shell component. Although low, these limits on the radio emission are nonetheless compatible with a broad-band model of the X-ray emission.
3. The feature called the northern knot of G21.5–0.9 is clearly seen at 1.4 GHz. Its spectral index was $\alpha_{1.4\text{ GHz}}^{4.9\text{ GHz}} = -0.04 \pm 0.31$, similar to that of the remainder of G21.5–0.9, (i.e., $\alpha \simeq 0$), although a steeper value as is typical of shells is not excluded by the large uncertainties.

⁷ Available at <http://irsa.ipac.caltech.edu/data/SPITZER/GLIMPSE>

4. We detect a new shell SNR, G21.64–0.84. The shell has an angular diameter of $\sim 13'$. Only part of the shell is visible in our higher-resolution 1.4-GHz image, but it can be seen to have a double structure with what appears as two roughly concentric shells. The shell structure is clearly visible on a 327-MHz image, and the source has a total 327-MHz flux density of ~ 2.8 Jy. The source's spectral index is clearly non-thermal. No $8\ \mu\text{m}$ infrared or X-ray emission is seen.

5. A further extended radio source, G21.45–0.59, is visible to the west of G21.5–0.9, which we identify as a likely HII region due to the flat radio spectral index and its detection in the infrared.

ACKNOWLEDGEMENTS

M. F. Bietenholz, H. C. Matheson, S. Safi-Harb and N. Bartel acknowledge support by the Natural Sciences and Engineering Research Council (NSERC). S. Safi-Harb acknowledges support by the Canada Research Chairs program. This research made use of NASA's Astrophysics Data System.

REFERENCES

- Altenhoff W. J., Downes D., Goad L., Maxwell A., Rinehart R., 1970, *Astron. Astrophys. Suppl. Ser.*, 1, 319
- Bandiera R., Petruk O., 2010, *Astron. Astrophys.*, 509, A34
- Becker R. H., Kundu M. R., 1976, *ApJ*, 204, 427
- Becker R. H., Szymkowiak A. E., 1981, *ApJL*, 248, L23
- Benjamin R. A., Churchwell E., Babler B. L., Bania T. M., Clemens D. P., Cohen M., Dickey J. M., Indebetouw R., Jackson J. M., Kobulnicky H. A., Lazarian A., Marston A. P., Mathis J. S., Meade M. R., Seager S., Stolovy S. R., Watson C., Whitney B. A., Wolff M. J., Wolfire M. G., 2003, *PASP*, 115, 953
- Bietenholz M. F., Bartel N., 2008, *MNRAS*, 386, 1411
- Bietenholz M. F., Kassim N. E., Weiler K. W., 2001, *ApJ*, 560, 772
- Bocchino F., van der Swaluw E., Chevalier R., Bandiera R., 2005, *Astron. Astrophys.*, 442, 539
- Bock D. C.-J., Wright M. C. H., Dickel J. R., 2001, *ApJL*, 561, L203
- Brogan C. L., Gaensler B. M., Gelfand Y., Roberts M. E. E., Lazio T. J., Kassim N. E., 2005, in *X-Ray and Radio Connections* (eds. L.O. Sjouwerman and K.K. Dyer) Published electronically by NRAO, <http://www.aoc.nrao.edu/events/xrayradio> Held 3-6 February 2004 in Santa Fe, New Mexico, USA, (E4.09) 3 pages, L. O. Sjouwerman & K. K. Dyer, ed.
- Brogan C. L., Gelfand J. D., Gaensler B. M., Kassim N. E., Lazio T. J. W., 2006, *ApJL*, 639, L25
- Camilo F., Ransom S. M., Gaensler B. M., Slane P. O., Lorimer D. R., Reynolds J., Manchester R. N., Murray S. S., 2006, *ApJ*, 637, 456
- Chevalier R. A., 1982, *ApJL*, 259, L85
- Davelaar J., Smith A., Becker R. H., 1986, *ApJL*, 300, L59
- Frail D. A., Kassim N. E., Cornwell T. J., Goss W. M., 1995, *ApJL*, 454, L129
- Fürst E., Handa T., Morita K., Reich P., Reich W., Sofue Y., 1988, *PASJ*, 40, 347
- Gaensler B. M., 1998, *ApJ*, 493, 781
- Giaccani E., Smith M. J. S., Dubner G., Loiseau N., Castelletti G., Paron S., 2009, *Astron. Astrophys.*, 507, 841
- Gotthelf E. V., Helfand D. J., Newburgh L., 2007, *ApJ*, 654, 267
- Green D. A., 2004, *Bulletin of the Astronomical Society of India*, 32, 335
- , 2005, *Memorie della Societa Astronomica Italiana*, 76, 534
- , 2009, *Bulletin of the Astronomical Society of India*, 37, 45
- Gupta Y., Mitra D., Green D. A., Acharyya A., 2005, *Current Science*, 89, 853
- Jun B., Norman M. L., 1996, *ApJ*, 465, 800
- Kassim N. E., 1992, *AJ*, 103, 943
- Matheson H., Safi-Harb S., 2005, *Advances in Space Research*, 35, 1099
- , 2010, *submitted to ApJ*, ArXiv e-prints
- Morsi H. W., Reich W., 1987, *Astron. Astrophys. Suppl. Ser.*, 69, 533
- Reich W., Fuerst E., Arnal E. M., 1992, *Astron. Astrophys.*, 256, 214
- Reich W., Fuerst E., Haslam C. G. T., Steffen P., Reif K., 1984, *Astron. Astrophys. Suppl. Ser.*, 58, 197
- Reynolds S. P., 1998, *ApJ*, 493, 375
- Reynolds S. P., Aller H. D., 1985, *AJ*, 90, 2312
- Safi-Harb S., Harrus I. M., Petre R., Pavlov G. G., Koptsevich A. B., Sanwal D., 2001, *ApJ*, 561, 308
- Salter C. J., Reynolds S. P., Hogg D. E., Payne J. M., Rhodes P. J., 1989, *ApJ*, 338, 171
- Slane P., Chen Y., Schulz N. S., Seward F. D., Hughes J. P., Gaensler B. M., 2000, *ApJL*, 533, L29
- Stil J. M., Taylor A. R., Dickey J. M., Kavars D. W., Martin P. G., Rothwell T. A., Boothroyd A. I., Lockman F. J., McClure-Griffiths N. M., 2006, *AJ*, 132, 1158
- Tammann G. A., Loeffler W., Schroeder A., 1994, *ApJS*, 92, 487
- Warwick R. S., Bernard J.-P., Bocchino F., Decourchelle A., Ferrando P., Griffiths R. G., Haberi F., La Palombara N., Lumb D., Mereghetti S., Read A. M., Schaudel D., Schurch N., Tiengo A., Willingale R., 2001, *Astron. Astrophys.*, 365, L248
- Wilson A. S., Weiler K. W., 1976, *Astron. Astrophys.*, 49, 357
- Yamauchi S., Koyama K., Tomida H., Yokogawa J., Tamura K., 1999, *PASJ*, 51, 13